Power Electronic Systems
Laboratory

IEEE Transactions on Industrial Electronics, Vol. 63, NO. 6, pp. 3489-3498, June 2016

New Position-Sensing Concept for Miniature Lateral-Stator Machines

A. Tüysüz,
J. W. Kolar

Eidgenössische Technische Hochschule Zürich
Swiss Federal Institute of Technology Zurich

New Position-Sensing Concept for Miniature Lateral-Stator Machines

Arda Tüysüz, *Member, IEEE*, and Johann W. Kolar, *Fellow, IEEE*

***Abstract*—Lateral-stator machine (LSM) is an unconventional permanent-magnet electrical machine type that enables direct drive for micromachining applications where the space in the tool head is limited. In such applications, standard position sensors cannot be used due to the space limits. The back electro-motive force (EMF) cannot be used for position estimation as the rotor position is needed over the full-speed range, including very low speeds. Moreover, the load-dependent saturation of the stator core hinders an impedance-tracking-based self-sensing approach. Therefore, this paper presents integrated position sensors comprising sensing coils wound on the shielding iron, which is a part specific to the mentioned type of machine. Using this approach, the challenge introduced by the specific machine geometry is turned into an opportunity to realize highly compact and robust position sensors that can operate from standstill up to 200 000 r/min. Measurement results prove the validity of the design procedure. Even though developed for a specific type of electric machine, the presented approach can be used for position sensing of other types of electromechanical actuators.**

***Index Terms*—High-speed drives, lateral-stator machine (LSM), position sensing, sensing coils, speed sensing.**

I. Introduction

ROTOR position of a permanent-magnet synchronous machine (PMSM) needs to be known for a closed-loop operation. Position sensors such as encoders or resolvers can be used to obtain the rotor position information [1], [2]. However, these sensors not only require additional space but also increase the cost and the complexity, and decrease the overall reliability of the drive system. For that reason, drives without position sensors (self-sensing drives) have been gaining an increasing attention from both academia and industry. The back electromotive force (EMF) can be used to estimate the rotor position at high speeds, whereas the variation in the machine impedance with the rotor position can be exploited for position estimation also at lower speeds [3]–[5]. In [6] and [7], signal injection methods are presented for estimating the rotor potion based on its relationship with the self and mutual winding inductances. The authors of [8] discuss the position estimation errors for a signal-injection-based position-sensing algorithm where an analog filter is utilized to read out the machine's response to the injected signal. The injection of multiple high-frequency signals with different frequencies and amplitudes is proposed in [9], in order to increase the self-sensing capability of PMSMs with surface-mounted permanent magnets and concentrated windings. The self-sensing capability of an electric machine can also be enhanced by modifications in the structure of the machine [10], which is analyzed for induction machines in [5], for PMSMs in [11] and for synchronous reluctance machines in [12].

The lateral-stator machine (LSM) is presented in [13] for applications such as dental drills, where a wide speed and torque range is required and the space for the electric machine is strictly limited. The LSM topology can be seen in Fig. 1(a). As shown in Fig. 1(b), in a state-of-the-art dental handpiece, an electric machine with a rated speed of around 40 000 r/min is placed in the body of the handpiece, where the available space is larger. Several stages of mechanical transmission are used to connect the machine to the drill and to increase the speed up to around 200 000 r/min at the same time. A high-speed machine placed directly at the head of the dental handpiece would enable a direct drive and omit the need for mechanical transmissions; however, the space at the tool head is small and a state-of-the-art electrical machine fitting there could not deliver the torque required by the application (>5 mNm). However, an LSM as shown in Fig. 1(c) can fit in the tool head and drive the drill directly. Due to the peculiar shape of its stator extending laterally only on one side, the LSM makes use of the space at the tool neck, which would not be used for magnetic parts in case of conventional machine geometries.

A signal-injection-based self-sensing method is presented for the LSM in [14], where dedicated hardware injects a high-frequency current in the machine and the voltage response of the machine is measured and used for estimating the rotor position. On the other hand, Fig. 2 shows all the self and mutual inductances in dependency of the rotor position, for the LSM that is the outcome of the optimization procedure described in [13]. All the self and mutual inductances go flat at the same rotor position, making an impedance-tracking-based self-sensing method go blind at these rotor positions. Furthermore, the dependency of the inductances on the rotor position is heavily influenced by the load of the machine due to the saturation of the stator core. Hence, it can be concluded that an LSM optimized for highest torque and lowest losses is not necessarily suitable for self-sensing position estimation at the full-speed range (0–200 000 r/min).

In this paper, a new position estimation method is proposed for the LSM. Sensing coils are introduced in the machine and a

Manuscript received July 16, 2015; revised October 20, 2015; accepted November 16, 2015. Date of publication February 16, 2016; date of current version May 10, 2016.

The authors are with the Power Electronic Systems Laboratory, Swiss Federal Institute of Technology (ETH Zurich), CH-8092 Zurich, Switzerland (e-mail: tuysuz@lem.ee.ethz.ch; kolar@lem.ee.ethz.ch).

Color versions of one or more of the figures in this paper are available online at http://ieeexplore.ieee.org.

Digital Object Identifier 10.1109/TIE.2016.2530791

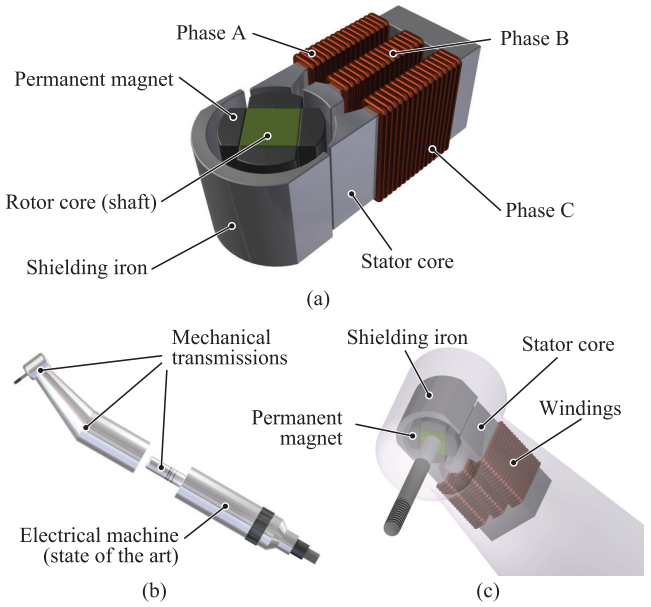

Fig. 1. (a) Conceptual drawing of the lateral-stator machine (LSM). In the prototype analyzed in this work, the lateral stator and the shielding iron are made of amorphous iron with 23-μm lamination thickness, and the shaft is made of a solid magnetic steel. The rotor magnets are sintered NdFeB magnets with 1.1 T remanent flux density. A retaining sleeve is used to hold the magnets in their position at high speeds (not shown in this figure). The shielding iron is used for guiding the flux of the permanent magnets that are not facing the stator core. (b) State-of-the-art electric dental handpiece. The rated speed of the electrical machine is around 40 000 r/min. Mechanical step-up transmission stages are used to connect the machine to the drill, whose rated speed is 200 000 r/min. (c) LSM fits in the tool head and can deliver the required torque without using gearboxes. As the stator core is extended on one lateral side, space is gained for the windings outside the tool head.

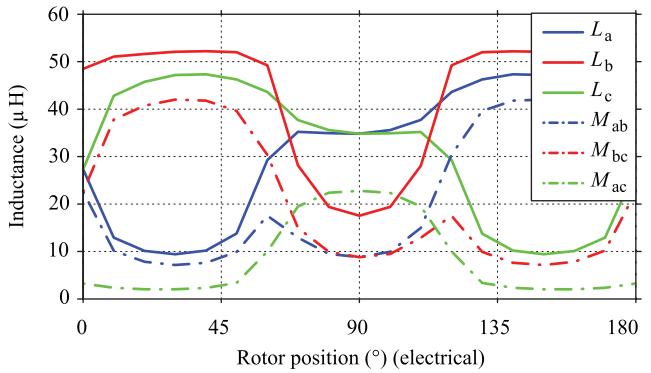

Fig. 2. Results of 2-D finite-element method (FEM) analysis showing the self and mutual inductances of the LSM optimized in [13]. L denotes self and M denotes mutual inductances. a, b, and c denote different machine phases.

high-frequency signal is injected in these coils to measure their impedances, which depend on the rotor position. Even though this method cannot be called self-sensing, it omits the additional space requirements of the above-mentioned position sensors by integrating the position sensors into the machine. As it will be shown later, only a $0.2\,\mathrm{mm} \times 0.3\,\mathrm{mm}$ slot is enough to accommodate a sensing coil in the considered machine, which is smaller than what would be necessary for standard position sensors such as a Hall effect sensor. Furthermore, sensing coils can survive the high temperatures ($>100\,^{\circ}\mathrm{C}$) required for the

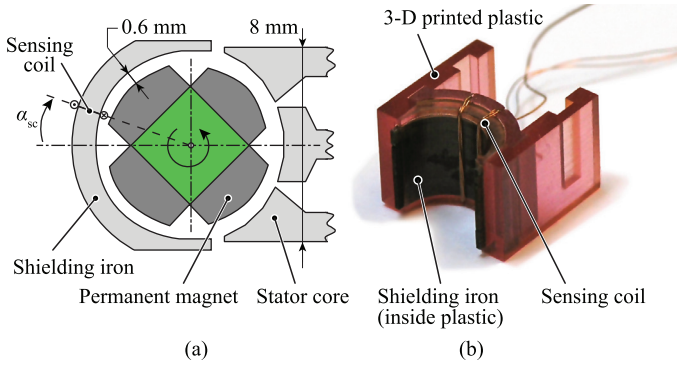

Fig. 3. (a) Schematic representation of an LSM with a sensing coil wound around the shielding iron. The permanent magnets are glued onto the shaft (shown in green) which is machined out of a solid piece of magnetic steel. In order to hold them on the shaft at high speeds, a retaining sleeve is used, but not shown in this figure for simplicity. In the machine prototype analyzed in this work, the magnetic air gap is 0.6 mm. Considering the plastic case on the stator side and the sleeve on the rotor, the actual (mechanical) air gap is 0.2 mm. (b) Photo of a shielding iron with two sensing coils wound on it. The iron is placed inside a 3-D printed plastic case that facilitates the positioning of the shielding iron and the winding of the sensing coil.

sterilization of dental handpieces. The proposed method also decouples the position estimation from the load of the machine, making it operational over a wide load range.

The use of sensing coils for position estimation is also shown in [15], where the rotor position is extracted using the voltage induced in the sensing coils due to the rotor's movement. On the other hand, as the impedance of the sensing coils is measured in this work instead of the induced voltage, the method presented in this work can be used also at lower speeds, including standstill. Thus, it is a robust method that is insensitive not only to the load but also to the speed of the machine.

II. Concept Description

The shielding iron is an inherent part of the presented LSM. It is needed to guide the flux of the magnets that are not facing the stator, such that the magnetic fields stay in a confined and controlled space. Even though it does not effect the mean torque capability of the machine, the geometry of the shielding iron may change the cogging torque and the magnetic pull acting on the rotor, as it changes the field distribution around the rotor.

Sensing coils can be wound on the shielding iron as shown in Fig. 3(a). The position of a sensing coil α_{sc} can be chosen freely as long as the mechanical construction permits, which is not the case when the machine phases are used for position sensing in a self-sensing approach. Furthermore, as seen in Fig. 4, the magnetic circuit is nearly not influenced by the field generated by the drive currents, which means that the rotor position estimation is not significantly affected by the load. On the other hand, the sensing coils increase the complexity of the machine production and increase the number of total cables between the machine and the inverter.

2-D FEM simulations are used to calculate the inductance L_{sc} of a sensing coil placed at different angles α_{sc} for different rotor positions. Fig. 5 shows the self inductances of the

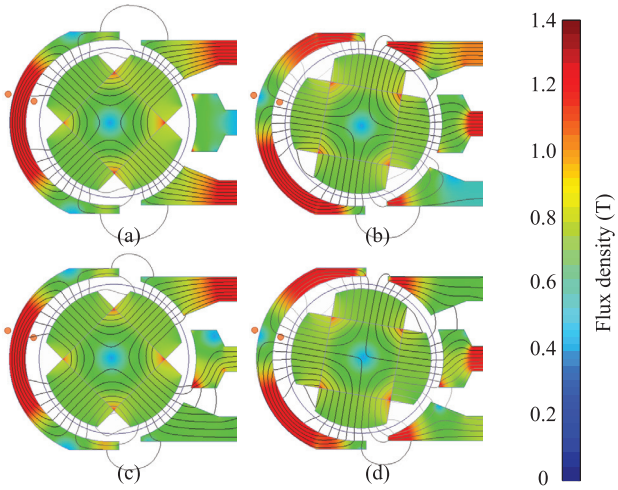

Fig. 4. 2-D FEM simulations showing the field distribution in the shielding iron and the tips of the stator legs of the analyzed LSM. Rotor is at 0° (electrical) in (a) and (c) and at 70° (electrical) in (b) and (d). (a) and (b) No-load and (c) and (d) full-load condition. The sensing coil is placed at $\alpha_{sc} = 15°$ in all cases. It can be seen that the field distribution in the shielding iron depends mainly on the rotor position and is not significantly affected by the machine's load.

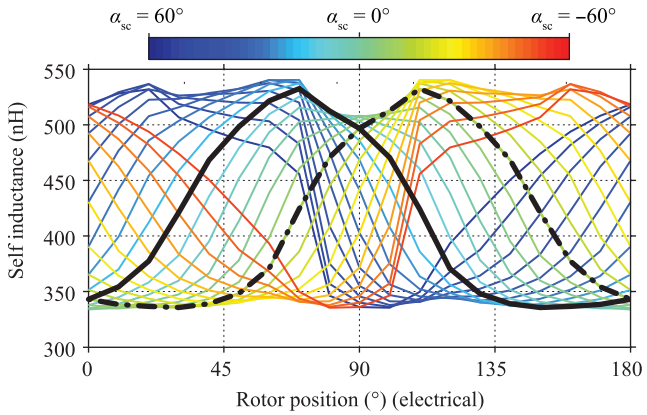

Fig. 5. 2-D FEM analysis results showing the self inductances of the sensing coils placed at positions from -60° to 60°. Solid and dashed black lines show $\alpha_{sc} = 15°$ and $\alpha_{sc} = -15°$.

sensing coils wound between $\alpha_{sc} = -60°$ and $\alpha_{sc} = 60°$ with 10° steps, when the number of turns is 5. It can be seen that the inductances of the coils at $\alpha_{sc} = -15°$ and $\alpha_{sc} = 15°$ can be used for estimating the rotor position as well as the direction of rotation.

The shape of the curves shown in Fig. 5 can be better understood by looking at Figs. 5 and 4 together. The inductance L_{sc} of a sensing coil is at its minimum when the permanent-magnet field pushes the part of iron under the sensing coil into saturation; contrarily, it is at its maximum when the iron underneath is furthest away from saturation.

As the waveforms have double the electrical frequency, they cannot be used to estimate the initial rotor position. In applications where the machine is not loaded at the start-up, the inverter can set the initial rotor position, whereas an initial rotor-position-sensing method that utilizes the saturation in the stator core or the shielding iron can be implemented in applications where this is not possible.

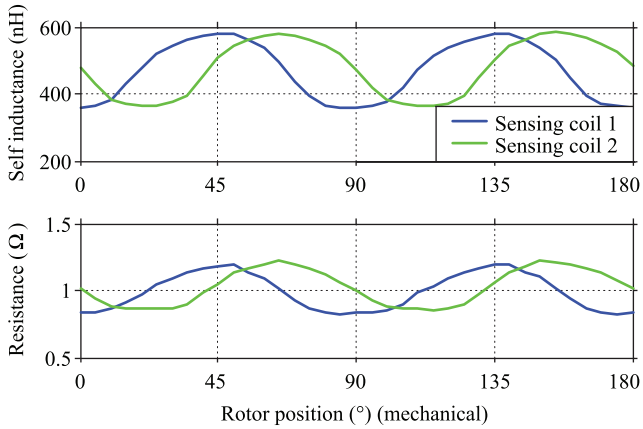

Fig. 6. Series resistance R_{sc} and self inductance L_{sc} of the sensing coils measured at 1 MHz using an Agilent 4294A impedance analyzer.

III. Hardware Realization of Sensing Coils

Fig. 3(b) shows a photo of the sensing coils wound around the shielding iron. The shielding iron is placed inside a 3-D printed plastic case that facilitates the positioning of the shielding iron with respect to the stator core and the rotor of the LSM. Two $0.2\ \text{mm} \times 0.3\ \text{mm}$ slots are present on the plastic case in which the sensing coils are placed. Each sensing coil has five turns. The shielding iron is made of amorphous iron with 23-μm-thick laminations. The rotor magnets are sintered NdFeB magnets with a remanent flux density of 1.1 T. The shaft is made of a solid cobalt-iron steel.

After winding the two sensing coils on a shielding iron, an impedance analyzer (Agilent 4294A) is used to measure the impedance Z_{sc} of the sensing coils at different rotor positions at standstill. Fig. 6 shows the resistance R_{sc} and inductance L_{sc} of the sensing coils when the sensing coil is modeled using a series R-L circuit, such that the measured impedance is $Z_{sc} = R_{sc} + j\omega_{ia}L_{sc}$, $\omega_{ia} = 2\pi f_{ia}$, and $f_{ia} = 1\,\text{MHz}$.

The measurement results show that the 2-D FEM simulations were able to predict the variation in the sensing-coil inductance L_{sc} with the rotor position accurately. The measurement results also show that the sensing-coil resistance R_{sc} also changes with the rotor position, and its dependency on the rotor position follows that of the L_{sc}. The measured coil resistance R_{sc} consists not only of the resistance of the copper wire, but it also reflects the losses generated by the measurement signal in the shielding iron (core losses) and the rotor (eddy-current losses) at the injection frequency. If the injection frequency is constant, the core and eddy-current losses change with the rotor position, making R_{sc} a function of the rotor position.

IV. Design of Sensor Electronics

Fig. 7 shows a functional block diagram of the sensor electronics. A digital signal processor (DSP) is used to generate a rectangular signal $u_{dsp,inj}$ with frequency f_{inj}. This signal is low-pass filtered using an active filter, which also acts like a buffer and provides the sinusoidal injection current i_{sc} with the same frequency. The capacitor C_{hf} is used to block the dc and the low-frequency components, whereas an R_{lim} with sufficiently

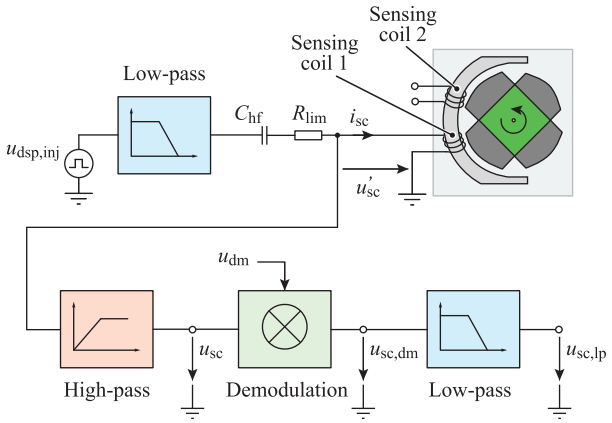

Fig. 7. Block diagram of the high-frequency signal injection, measurement, filtering, and demodulation for rotor position estimation using sensing coils. Only the injection/measurement channel connected to one sensing coil is shown for simplicity. An identical channel is connected to the second sensing coil. Using separate channels enables choosing injection and demodulation signals with arbitrary phase displacement.

high resistance limits the current and makes the system behave as a high-frequency current source. The sensing coil voltage u'_{sc} is high-pass filtered in order to remove the induced voltage in the coil due to the rotation of the permanent-magnet field (back EMF). Resulting voltage u_{sc} contains rotor position information. This information can be extracted by a DSP that samples the signal $u_{sc,lp}$, which is yielded after u_{sc} is demodulated and low-pass filtered. The injection and measurement channel described here is built twice as there are two sensing coils wound on the shielding iron, i.e., the signal injection, filtering, and demodulation stages for the two sensing coils are separate but identical.

In such a configuration, the voltages measured at the terminals of the sensing coils $u'_{sc,1}$, $u'_{sc,2}$ can be expressed as

$$u'_{sc,1}(t,\theta) = i_{sc,1}(t)R_{sc,1}(\theta) + L_{sc,1}(\theta)\frac{di_{sc,1}(t)}{dt} + M_{sc}(\theta)\frac{di_{sc,2}(t)}{dt} + e_{sc,1}(t) \quad (1)$$

$$u'_{sc,2}(t,\theta) = i_{sc,2}(t)R_{sc,2}(\theta) + L_{sc,2}(\theta)\frac{di_{sc,2}(t)}{dt} + M_{sc}(\theta)\frac{di_{sc,1}(t)}{dt} + e_{sc,2}(t) \quad (2)$$

where t is time, θ is the rotor position, M_{sc} is the mutual inductance between the two sensing coils, $i_{sc,1}$ and $i_{sc,2}$ are the currents, and $e_{sc,1}$ and $e_{sc,2}$ are the back EMFs in the first and second sensing coils, respectively.

The high-pass filter suppresses the back EMFs due to their low frequencies; therefore, $e_{sc,1}$ and $e_{sc,2}$ are not considered any further in the analysis. As only sinusoidal injection currents are considered, and the amplitudes of the injected currents are too small to lead to any saturation-related distortions in the voltage response of the machine (i.e., L_{sc} changes only with rotor position and not with injected current), the voltage drops on the coil resistances and inductances are sinusoidal and 90° phase shifted. This means that the phase angle of the demodulation signal u_{dm} is a degree of freedom on how to synthesize the voltage $u_{sc,dm}$ that will be sampled by the DSP after being low-pass filtered.

This can be explained easily on a setup with only one sensing coil and no back EMF, where the measured and high-pass filtered sensing-coil voltage can be written as

$$u_{sc}(t,\theta) = \hat{i}_{sc}R_{sc}(\theta)\cos(\omega_{inj}t) + \hat{i}_{sc}\omega_{inj}L_{sc}(\theta)\cos\left(\omega_{inj}t - \frac{\pi}{2}\right). \quad (3)$$

A well-known method to extract the amplitude of a sinusoidal signal with a defined frequency is multiplication with a sinusoidal demodulation signal with the same frequency. This results in a demodulated signal containing a dc component and a high-frequency component with twice the frequency of the demodulation signal. A low-pass filter can be used to suppress the high-frequency component, yielding in a dc signal proportional to the amplitude of the initial sinusoidal signal. Assuming a demodulation signal in the form $u_{dm}(t) = \cos(\omega_{inj}t - \phi_{dm})$ where ϕ_{dm} is the demodulation angle, the demodulated signal u_{dm} can be written as

$$u_{sc,dm}(t) = u_{sc}(t)u_{dm}(t) \quad (4)$$

$$u_{sc,dm}(t,\theta) = \left(\hat{i}_{sc}R_{sc}(\theta)\cos(\omega_{inj}t) + \hat{i}_{sc}\omega_{inj}L_{sc}(\theta)\cos(\omega_{inj}t - \frac{\pi}{2})\right)\cdot\cos(\omega_{inj}t - \phi_{dm}) \quad (5)$$

$$u_{sc,dm}(t,\theta) = \hat{i}_{sc}R_{sc}(\theta)A + \hat{i}_{sc}\omega_{inj}L_{sc}(\theta)B \quad (6)$$

where

$$A = \frac{\cos(2\omega_{inj}t - \phi_{dm})}{2} + \frac{\cos(\phi_{dm})}{2} \quad (7)$$

and

$$B = \frac{\cos(2\omega_{inj}t - \frac{\pi}{2} - \phi_{dm})}{2} + \frac{\cos(\phi_{dm} - \frac{\pi}{2})}{2}. \quad (8)$$

As the low-pass filter suppresses the components of A and B that oscillate with twice the injection frequency, the low-pass filtered signal $u_{sc,lp}$ is expressed as

$$u_{sc,lp(\theta)} = \hat{i}_{sc}R_{sc}(\theta)\frac{\cos(\phi_{dm})}{2} + \hat{i}_{sc}\omega_{inj}L_{sc}(\theta)\frac{\cos(\phi_{dm} - \frac{\pi}{2})}{2}. \quad (9)$$

Since $u_{sc,lp}$ does not contain any injection-frequency components, its sampling by the DSP does not need to be synchronized with the injection, and the sampling frequency can be significantly lower than the injection frequency. In practice, assuming that the DSP can generate a new rotor position estimate for each sample, the sampling frequency can be the same as the inverter switching frequency, in order to update the rotor position information for each inverter switching cycle.

Moreover, it can be concluded from (9) that the demodulation angle ϕ_{dm} can be used to read either the voltage drop on the coil resistance, or the voltage drop on the coil inductance, or a combination of both. Equations (3)–(9) are derived on a setup with one sensing coil, i.e., without any mutual coupling. However, when mutual coupling from a neighboring sensing

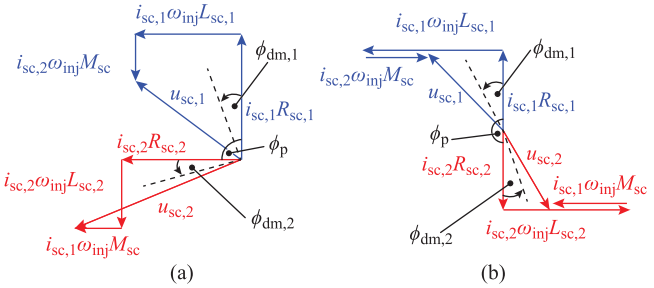

Fig. 8. Phasor diagram of the induced voltages in two sensing coils on one shielding iron due to the injected signals (back EMF is omitted). Blue and red denote voltages induced in different sensing coils. (a) Currents injected in the sensing coils are $\phi_p = 90°$ phase shifted . (b) Currents injected in the sensing coils are $\phi_p = 180°$ phase shifted.

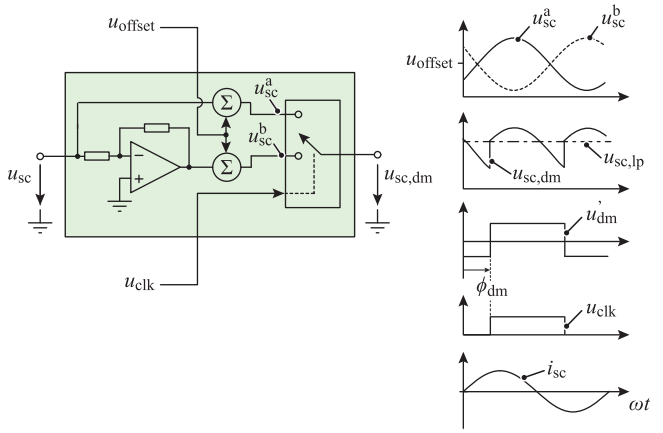

Fig. 9. Functional block diagram showing the multiplication of u_{sc} with a rectangular demodulation signal u'_{dm}. An inverting amplifier and an analog switch are used to perform the multiplication in hardware. The signals are shifted by a positive u_{offset} such that single-supply signal electronics can be used.

coil is present, depending on the phase angle ϕ_p between the injected currents, the demodulation angle ϕ_{dm} can be used to cancel the mutual coupling in a similar way.

Fig. 8(a) shows the phasor diagram of a case where $\phi_p = 90°$ phase-shifted currents are injected in two sensing coils with a mutual inductance M_{sc} between them. For each sensing coil, the demodulation angle ϕ_{dm} can be set independently depending on what quantity is to be read from that channel ($u_{sc,lp,1}$ and $u_{sc,lp,2}$ can be considered as the projections of the sensing-coil voltages $u_{sc,1}$ and $u_{sc,2}$ on the dashed lines). For example, in Fig. 8(a), $\phi_{dm,1} = 0$ leads to the reading of the difference of the voltage drop on the first coil's resistance and induced voltage across the mutual reactance ($u_{sc,lp,1} = i_{sc,1}R_{sc,1} - i_{sc,2}\omega_{inj}M_{sc}$); whereas $\phi_{dm,2} = 90°$ omits the resistive voltage drop and the mutual coupling, and leads to the reading of the voltage drop across the self inductance of the second coil only ($u_{sc,lp,2} = i_{sc,2}\omega_{inj}L_{sc,2}$).

Similarly, for the case shown in Fig. 8(b) where $\phi_p = 180°$, $\phi_{dm,1} = 0$ enables the measurement of only the resistive voltage drop on the first coil's resistance ($u_{sc,lp,1} = i_{sc,1}R_{sc,1}$), whereas $\phi_{dm,2} = 90°$ leads to the reading of the difference of the voltage drop across the self inductance of the second coil and the induced voltage across the mutual inductance ($u_{sc,lp,2} = i_{sc,2}\omega_{inj}L_{sc,2} - i_{sc,1}\omega_{inj}M_{sc}$).

The degree of freedom introduced by the independently adjustable ϕ_p, $\phi_{dm,1}$, and $\phi_{dm,2}$ enables the synthesis of the required waveform at the output of the demodulation stage, giving the designer the flexibility to shape the voltage $u_{sc,lp}$ sampled by the DSP. This may be used to maximize the rotor-position-sensing sensitivity for a given machine and sensing-coil geometry, as explained in the following sections.

So far, multiplication with a sinusoidal demodulation signal in the form $u_{dm}(t) = \cos(\omega_{inj}t - \phi_{dm})$ has been assumed for easier mathematical description of the demodulation process. Nevertheless, multiplication with a rectangular signal of the form

$$u'_{dm}(t) = \begin{cases} 1, & \cos(\omega_{inj}t - \phi_{dm}) \geq 0 \\ -1, & \cos(\omega_{inj}t - \phi_{dm}) < 0 \end{cases} \quad (10)$$

can also be used for the same purpose, and it is significantly easier to realize in hardware. As shown in Fig. 9, a simple inverting amplifier circuit and an analog switch can be used to perform the multiplication of $u_{sc}(t)$ with $u'_{dm}(t)$. Since the clock signal u_{clk} is a digital signal generated by the same DSP that generates the injection signal $u_{dsp,inj}$ (cf., Fig. 7), the demodulation angle ϕ_{dm} can be adjusted precisely in software. Moreover, the signals are shifted by a positive offset voltage u_{offset} for being able to use single-supply signal electronics.

V. Design Aspects

So far, it has been shown that the position of the sensing coil α_{sc}, the phase displacement between the injected currents ϕ_p, and the demodulation angles $\phi_{dm,1}$, $\phi_{dm,2}$ all influence the shape of the signal $u_{sc,lp}$, which contains the rotor position information. Clearly, the set of these parameters needs to be selected such that the DSP that samples the resulting $u_{sc,lp}$ of different sensing coils can estimate the rotor position based on these voltages at all rotor positions, preferably in a computationally efficient way such as using look-up tables (LUTs). That is, the voltages should not go flat or reach their maxima/minima at the same rotor position. Clearly, the proper selection of these parameters depends strictly on the application, and a universally optimum set of parameters cannot be defined. Nevertheless, the above-mentioned design parameters are discussed here along with several other design aspects in order to give the readers guidelines for applying the proposed method in various position-sensing applications.

The position α_{sc} of a sensing coil is obviously the first degree of freedom in order to modify the dependency of its impedance on the rotor position. However, mechanical constraints may limit where the sensing coil can be placed. In such a case, ϕ_p, $\phi_{dm,1}$, and $\phi_{dm,2}$ can be modified in order to modify $u_{sc,lp}$. As a different example, an application can be considered where the iron is not pushed deeply into saturation by the permanent-magnet flux. The self and mutual inductances of the sensing coils then do not depend strongly on the rotor position, but depending on the position of the sensing coil with respect to the conductive bodies in the rotor, the eddy-current losses induced in the rotor may lead to a rotor-position-dependent sensing-coil resistance. This can be read without the effect

of the sensing-coil inductance as shown in Fig. 8, by setting $\phi_{\mathrm{p}} = 180°$ and $\phi_{\mathrm{dm},1} = \phi_{\mathrm{dm},2} = 0°$. Different $u_{\mathrm{sc,lp}}$ measurements taken for different combinations of ϕ_{p}, $\phi_{\mathrm{dm},1}$, and $\phi_{\mathrm{dm},2}$ are presented in Section VI, for the LSM considered in this work.

In order to maintain a continuous rotor position sensing and to estimate the direction of rotation, at least two sensing coils are required. A higher number of sensing coils can be implemented in order to have redundancy, but the additional manufacturing effort and the space limits need to be considered.

The number of turns of a sensing coil, as in windings of electric machines, changes the ratio of current and voltage supplied by the driving electronics. However, as the power consumption of the sensor electronics is typically much lower than the drive power, this has almost no practical importance. A higher number of turns mean smaller wire radius for a given slot area, and in small systems such as the LSM analyzed in this work (with $0.06\ \mathrm{mm}^2$ slot area), a practical limit exists on the thinnest wire that can be used without a complicated winding method. On the other hand, the lead wires of the sensing coils add a rotor-position-independent offset to the sensing-coil impedance, whose ratio to the rotor-position-dependent impedance can be decreased by using a high number of turns. Twisting of the lead wires further decreases this impedance offset.

Injection frequency f_{inj} has to be selected sufficiently higher than highest frequency component of the back EMF induced in the sensing coils at the maximum rotor speed, such that the back EMF could be filtered out. Moreover, it has to be considered that the impedance Z_{sc} of a sensing coil depends on f_{inj} as its inductance L_{sc} decreases and the resistance R_{sc} increases with increasing f_{inj}, and the resulting $u_{\mathrm{sc,lp}}$ waveform should have sufficient dependency on the rotor position. Even though the magnetic circuit is decoupled from the drive currents, parasitic coupling may occur when the signal and power electronics share the same circuit board, which should also be considered when selecting f_{inj} with respect to the inverter's switching frequency and/or drive current measurement sampling frequency in order to avoid any possible parasitic crosstalk. Finally, with higher f_{inj} values in the MHz range, radiated EMI compliance specifications may need to be considered depending on the application.

The magnetic material on which a sensing coil is wound has a significant effect on its impedance. In the application presented in this work, the shielding iron is an inherent part of the LSM, and it is made of 23-μm-thick laminated amorphous iron sheets due to the low losses and high-saturation flux density of this material. However, in applications where the magnetic material that carries the sensing coils can be freely selected, the designer should consider the permeability and the core losses of the material at the injection frequency as well as at the maximum electrical frequency of the rotor in order to guarantee a position-dependent impedance at all rotor speeds, without unfeasibly high core losses.

Finally, the corner frequency of the low-pass filter has to be selected to pass all the significant harmonics of the $u_{\mathrm{sc,lp}}$ at the highest rotor speed. For example, considering the waveform shown with the solid line in Fig. 5, up to the sixth harmonic need to be considered, which occurs at 80 kHz when the machine speed is 200 000 r/min.

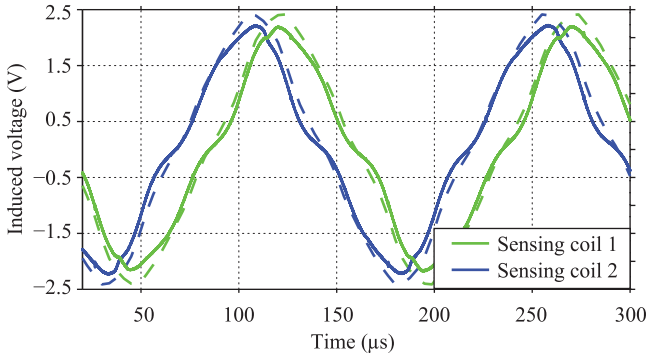

Fig. 10. Measured and simulated back EMF at 200 000 r/min. Solid lines show measured and dashed lines show simulated waveforms.

VI. Experimental Analysis

The signal electronics described in Section IV are realized in hardware to verify the design procedure. However, after the low-pass filters, simple analog subtraction and gain stages are utilized with variable resistors and operational amplifiers in order to be able to shift and scale the signals easily during measurements. In this section, the signals noted as $u_{\mathrm{sc,lp}}$ are demodulated and filtered as described earlier; additionally, they are shifted and scaled before being measured. The final variable shifting and scaling stage makes the hardware suitable for testing different sensing coils and different demodulation strategies, and it can be omitted in a final design where the sensing coil and the demodulation type are defined. A digital oscilloscope is used to measure $u_{\mathrm{sc,lp}}$ waveforms for different combinations of ϕ_{p}, $\phi_{\mathrm{dm},1}$, and $\phi_{\mathrm{dm},2}$, for verifying the signal injection, filtering, and demodulation steps described earlier. Finally, a simple method is shown at the end of this section as an example of how a DSP sampling the voltage $u_{\mathrm{sc,lp}}$ can determine the rotor position based on the measured voltage waveforms.

A commercially available high-speed (500 000 r/min) PMSM [16], which is driven in a self-sensing, closed-loop speed control by an off-the-shelf 400 W inverter [17], is mechanically coupled to the LSM and is used to drive the LSM for the experiments presented here. Details on the LSM used in this work and the test setup are given in [13]. For experiments under load, a three-phase resistive load is connected directly across the stator terminals of the LSM.

Even though a precise estimation of the back EMF in the sensing coils is not directly needed for rotor position estimation, the expected back EMF needs to be known in order to design the high-pass filter properly. Fig. 10 shows the induced back EMF in the sensing coils when the rotor is rotating at 200 000 r/min. There is a very good correlation between the simulated and measured waveforms, which verifies the FEM model.

The simulation results for the self inductances of the two sensing coils placed at $\alpha_{\mathrm{sc},1} = 15°$ and $\alpha_{\mathrm{sc},2} = -15°$ as well as the mutual inductance between them can be seen in Fig. 11.

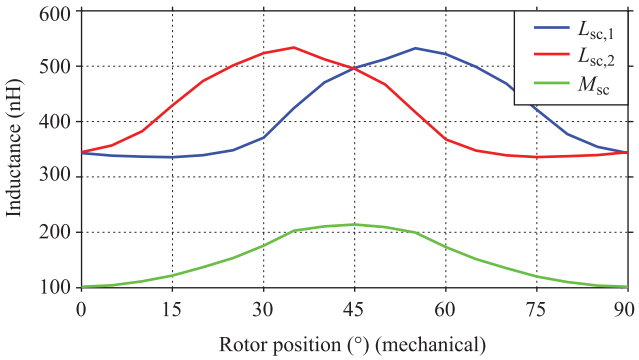

Fig. 11. 2-D FEM simulation results showing the self inductances $L_{sc,1}$ and $L_{sc,2}$ of the two sensing coils as well as their mutual inductance M_{sc}, for different rotor positions. The sensing coils are placed at $\alpha_{sc,1} = 15°$ and $\alpha_{sc,2} = -15°$, and they have 5 turns each.

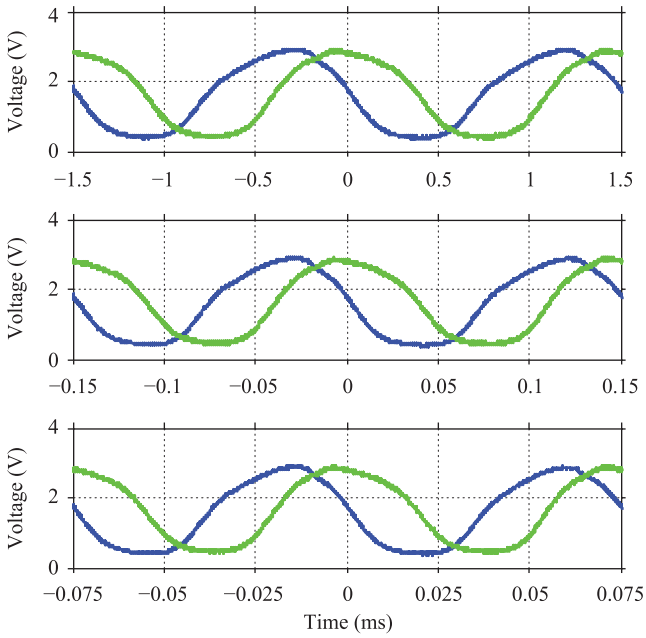

Fig. 12. Demodulated and filtered signal $u_{sc,lp}$, measured at three different speeds. Blue and green denote the signals from two different channels (two different sensing coils). (Top) 10 000 r/min. (Middle) 100 000 r/min. (Bottom) 200 000 r/min. The currents injected in the two sensing coils are $\phi_p = 90°$ phase shifted and the demodulation signals in both channels are adjusted to read only the self inductances and cancel out the resistive voltage drops and the effect of mutual coupling ($\phi_{dm,1} = \phi_{dm,2} = 90°$). The injection frequency is $f_{inj} = 1$ MHz.

A comparison of Figs. 11 to Fig. 6 reveals the validity of these simulation results. Fig. 12 shows $u_{sc,lp}$, the demodulated and filtered signal that is fed to the DSP, at 10 000 r/min (top), 100 000 r/min (middle), and 200 000 r/min (bottom) when the LSM is driven externally by a drive machine, under zero load. Fig. 13 displays $u_{sc,lp}$ when the machine is loaded by three star-connected resistors across its stator terminals. For these measurements, the injection frequency is $f_{inj} = 1$ MHz, the currents injected in the two sensing coils are $\phi_p = 90°$ shifted, and the demodulation signals in both channels are adjusted to read only the self inductances and cancel out the resistances and the mutual coupling ($\phi_{dm,1} = \phi_{dm,2} = 90°$, cf., Section IV). The waveform stays the same throughout the whole speed range,

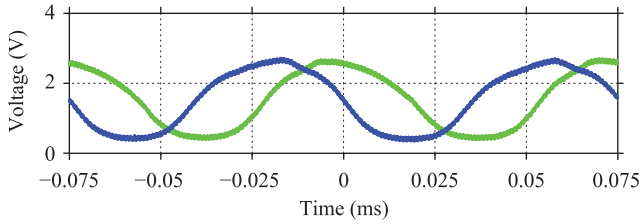

Fig. 13. Demodulated and filtered signal $u_{sc,lp}$, measured at 200 000 r/min and rated load. Blue and green denote the signals from two different channels (two different sensing coils). The currents injected in the two sensing coils are $\phi_p = 90°$ phase shifted and the demodulation signals in both channels are adjusted to read only the self inductances and cancel out the resistive voltage drops and the effect of mutual coupling ($\phi_{dm,1} = \phi_{dm,2} = 90°$). The injection frequency is $f_{inj} = 1$ MHz. The LSM is driven by an off-the-shelf drive machine and loaded with a three-phase resistive load connected across its stator terminals.

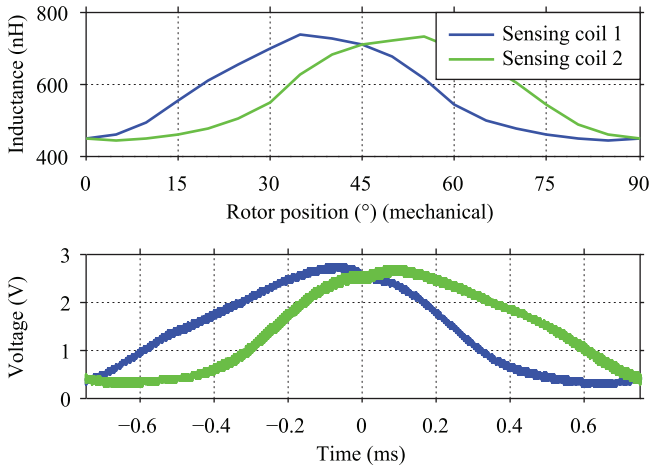

Fig. 14. Simulated and measured values for the sum of self and mutual inductances for two sensing coils. (Top) Simulated inductances. (Bottom) Measured voltage responses of the sensing coils after filtering and demodulation stages. In order to read the sum of self and mutual inductances and omit the resistive voltage drops, the currents in both sensing coils are in phase ($\phi_p = 0°$), and the demodulation angles are $\phi_{dm,1} = \phi_{dm,2} = 90°$. The machine speed is 10 000 r/min, the amplitude of the high-frequency currents injected in the machine are $\hat{i}_{sc} = 20$ mA, and the injection frequency is $f_{inj} = 1$ MHz.

which verifies the design of the filters. As clearly seen, the back EMF is successfully attenuated up to 200 000 r/min. A comparison to the simulated self inductances shown in Fig. 11 reveals that the waveforms look similar; hence, the effect of the mutual coupling is canceled out and the self inductances are read as intended.

Fig. 14 shows the simulated values for the sum of self and mutual inductances for both sensing coils in the top plot. In order to read the sum of self and mutual inductances without the resistive voltage drops, the currents in both sensing coils are in phase ($\phi_p = 0°$), and the demodulation angles are set as $\phi_{dm,1} = \phi_{dm,2} = 90°$. The bottom plot shows the resulting $u_{sc,lp}$, whose waveform is virtually identical to that of the simulation results shown in the top plot. The machine is rotating at 10 000 r/min, the amplitudes of the high-frequency currents injected in the machine are $\hat{i}_{sc} = 20$ mA, and the injection frequency is $f_{inj} = 1$ MHz.

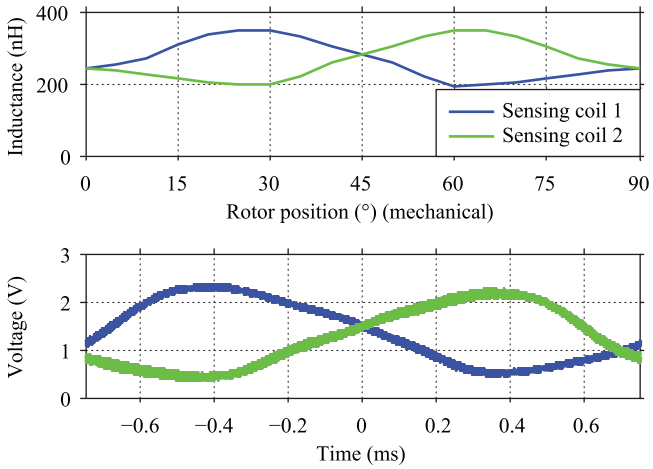

Fig. 15. Simulated and measured values for the difference of self and mutual inductances for two sensing coils. (Top) Simulated inductances. (Bottom) Measured voltage responses of the sensing coils after filtering and demodulation stages. In order to read the difference of self and mutual inductances and omit the resistive voltage drops, the currents in both sensing coils are $\phi_{\mathrm{p}} = 180°$ phase shifted, and the demodulation angles are $\phi_{\mathrm{dm},1} = \phi_{\mathrm{dm},2} = 90°$. The machine speed is 10 000 r/min, the amplitude of the high-frequency currents injected in the machine are $\hat{i}_{\mathrm{sc}} = 20$ mA, and the injection frequency is $f_{\mathrm{inj}} = 1$ MHz.

Finally, Fig. 15 shows the simulation results for the difference of self and mutual inductances for both sensing coils in the top, whereas the bottom plots shows the $u_{\mathrm{sc,lp}}$ that is shaped to follow the same waveform by injecting $\phi_{\mathrm{p}} = 180°$ phase-shifted high-frequency currents in the sensing coils and adjusting the demodulation angles as $\phi_{\mathrm{dm},1} = \phi_{\mathrm{dm},2} = 90°$. For this measurement, the machine speed is 10 000 r/min, the amplitudes of the high-frequency currents are $\hat{i}_{\mathrm{sc}} = 20$ mA, and the injection frequency is $f_{\mathrm{inj}} = 1$ MHz.

The rotor position information contained in these waveforms can be extracted by a DSP that samples these voltages using an analog-to-digital converter (ADC). Today, with the ever-increasing computational power and reducing cost of DSPs, one can think of several different algorithms for this task. Nevertheless, in low-power drives, signal and control electronics may still take up significant portion of the overall design effort and cost. Therefore, a position-sensing algorithm with very modest computational requirements is presented here as an example of how to extract the rotor position from measured voltages. The method makes use of LUTs employing index mapping and a few if–else statements, resulting in very simple digital calculations.

Fig. 16 shows simulated $u_{\mathrm{sc,lp}}$ values for $\phi_{\mathrm{p}} = \phi_{\mathrm{dm},1} = \phi_{\mathrm{dm},2} = 90°$, scaled considering an ADC that operates between 0 and 3 V, and a margin of 0.25 V from both voltage limits. When half of the electrical period is divided into four sectors as shown in Fig. 16, only two LUTs are enough as the sectors 1 and 3 as well as 2 and 4 are symmetrical. In order to keep the computational effort to a minimum, an 8-bit ADC is considered. In order to use index mapping, the voltage range 0.25–2.75V is divided into 2^7 equidistant voltage levels and the rotor position corresponding to these voltage levels in sectors 1 and 2 are stored in two LUTs. These LUTs are also shown in Fig. 16.

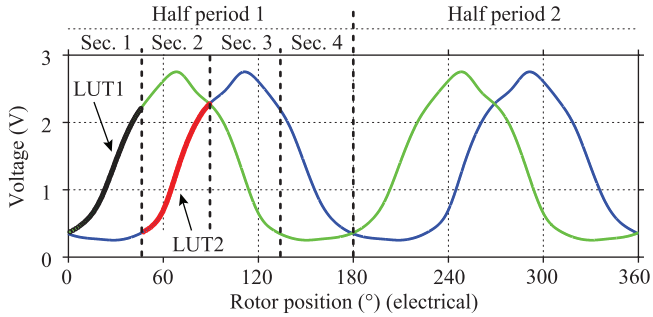

Fig. 16. Four sectors in an electrical half period and two LUTs that are used to estimate the rotor position.

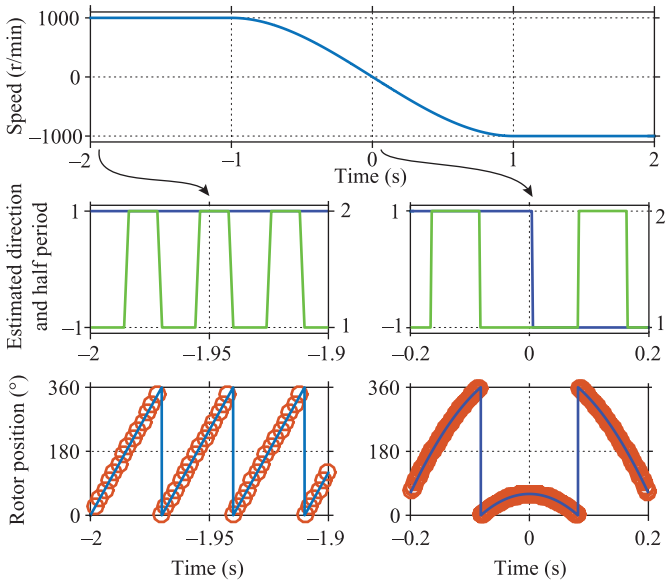

Fig. 17. Simulation results showing the validity of the proposed position-sensing algorithm. (Top) Assumed speed profile. (Middle) Estimated direction in blue and half period in green. (Bottom) Actual and estimated rotor position in electrical degrees. Estimated positions are denoted with circles.

The measured voltages (ADC results) can be used to detect the sector, and once the sector is known, the direction of rotation can be obtained by comparing the sampled voltage to the previous ADC result. Assuming that the initial position is known, the algorithm can detect the half period based on the direction of rotation and the sequence of the estimated sector numbers. Finally, the most significant 7 bits of the ADC results is used with the LUTs to estimate the position within a sector. It has to be noted that the 0 and 3 V range is divided into 2^7 steps such that the most significant 7 bits of the ADC results can be used for index mapping, but only 80 of these steps are within 0.36 and 2.27 V, which is the relevant range for the LUTs as shown in Fig. 16. Therefore, only 160 data points need to be stored by the DSP.

The proposed algorithm is verified with simulations using the commercial numerical computing software MATLAB. First, the speed profile shown in Fig. 17 (top) is assumed, and $u_{\mathrm{sc,lp},1}$ and $u_{\mathrm{sc,lp},2}$ are calculated such that they change between 0.25 and 2.75 V. Since a test case with low speeds and speed reversal is considered for verification at this stage, a rather low ADC

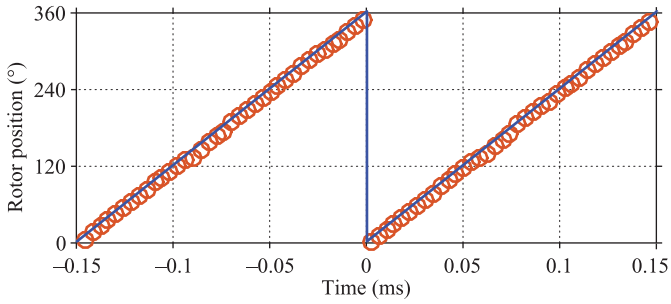

Fig. 18. Simulation results showing the application of the LUTs to extract the rotor position based on the measured signals. Actual (line) and estimated (circles) rotor positions in electrical degrees, based on the voltages shown in Fig. 12 (bottom), when the speed is 200 000 r/min.

sampling frequency of 500 Hz is adequate. A 2-μs delay is assumed in the simulations to account for the time required for the ADC and the following digital comparison and indexing operations carried out by the DSP. Fig. 17 shows that the proposed algorithm is able to track the rotor position accurately during constant speed operation, deceleration, speed reversal, and acceleration.

Finally, Fig. 18 shows the same method being applied to the measured voltage waveforms shown in Fig. 12 (bottom). Again, MATLAB is used to simulate the ADC and the following digital operations done by the DSP. An ADC sampling frequency of 250 kHz is considered and a delay of 2 μs is assumed in the simulation to account for ADC and the following digital operations. The LUTs have in total 160 entries, resulting in a mere 160-byte memory requirement for the DSP when 8-bit data points are considered.

VII. Conclusion

This paper presents robust and compact integrated position sensors that can operate from standstill up to 200 000 r/min for a special type of high-speed electric machine where the state-of-the-art self-sensing methods cannot be applied due to the unsuitable dependency of winding impedances on the rotor position, and the use of position sensors is not possible due to the strict space limitations.

Sensing coils are placed on the shielding iron, which is an inherent part of the LSM, the electrical machine topology considered in this work. A high-frequency signal is injected in the sensing coils in order to continuously track their impedances, which contain rotor position information. As the magnetic circuit of the sensing coils is not significantly influenced by the armature fields, the impedance of a sensing coil varies mainly with the rotor position and not with the machine load. Moreover, the position of the sensing coils can be chosen freely (within the available space), such that the dependency of the impedance on the rotor position can be modified.

Not only the position of the sensing coils on the shielding iron but also the phase displacement between the high-frequency currents injected in them, and the demodulation strategy can be adjusted in order to shape how the resulting voltage response of the sensing coils varies with the rotor position. This feature of the proposed method can be very useful in applications where the position of the sensing coils may not be freely chosen, e.g., due to mechanical constraints. Therefore, this paper not only presents a detailed description of how the proposed method is applied on a specific machine but also discusses various design aspects in order to offer the readers guidelines on how to apply the analyzed method in different applications.

Finally, the proposed method is verified with measurements at 10 000, 100 000, and 200 000 r/min and a simple algorithm based on LUTs is presented for rotor position extraction. In the future work, the presented method will be tested under dynamic (e.g., step) load conditions.

Acknowledgment

The authors would like to express their sincere appreciation to Celeroton AG for the continuous support they provided during the design, construction, and testing of the lateral-stator machine. The authors would also like to thank the support of CADFEM (Suisse) AG concerning the ANSYS software.

References

[1] T. Shi, Z. Wang, and C. Xia, "Speed measurement error suppression for PMSM control system using self-adaption Kalman observer," *IEEE Trans. Ind. Electron.*, vol. 62, no. 5, pp. 2753–2763, May 2015.

[2] Z. Zhang, F. Ni, Y. Dong, C. Guo, M. Jin, and H. Liu, "A novel absolute magnetic rotary sensor," *IEEE Trans. Ind. Electron.*, vol. 62, no. 7, pp. 4408–4419, Jul. 2006.

[3] F. Gabriel, F. De Belie, X. Neyt, and P. Lataire, "High-frequency issues using rotating voltage injections intended for position self-sensing," *IEEE Trans. Ind. Electron.*, vol. 60, no. 12, pp. 5447–5457, Dec. 2013.

[4] M. Schroedl, "Operation of the permanent magnet synchronous machine without a mechanical sensor," in *Proc. Intl. Conf. Power Electron. Variable Speed Drives*, Jul. 1990, pp. 51–56.

[5] P. L. Jansen and R. D. Lorenz, "Transducerless position and velocity estimation in induction and salient ac machines," in *Conf. Rec. IEEE Ind. Appl. Soc. Annu. Meeting*, Oct. 1994, pp. 488–495.

[6] J. Persson, M. Markovic, and Y. Perriard, "A new standstill position detection technique for nonsalient permanent-magnet synchronous motors using the magnetic anisotropy method," *IEEE Trans. Magn.*, vol. 43, no. 2, pp. 554–560, Feb. 2007.

[7] Z. Wang, S. Niu, S. L. Ho, W. N. Fu, and J. Zhu, "A position detection strategy for sensorless surface mounted permanent magnet motors at low speed using transient finite-element analysis," *IEEE Trans. Magn.*, vol. 48, no. 2, pp. 1003–1006, Feb. 2012.

[8] S. Jung and J.-I. Ha, "Analog filtering method for sensorless ac machine control with carrier frequency signal injection," *IEEE Trans. Ind. Electron.*, vol. 62, no. 9, pp. 5348–5358, Sep. 2015.

[9] Z. Chen, J. Gao, F. Wang, Z. Ma, Z. Zhang, and R. Kennel, "Sensorless control for SPMSM with concentrated windings using multisignal injection method," *IEEE Trans. Ind. Electron.*, vol. 61, no. 12, pp. 6624–6634, Dec. 2014.

[10] J.-I. Ha, "Analysis of inherent magnetic position sensors in symmetric ac machines for zero or low speed sensorless drives," *IEEE Trans. Magn.*, vol. 44, no. 12, pp. 4689–4696, Dec. 2008.

[11] R. Wrobel *et al.*, "Rotor design for sensorless position estimation in permanent-magnet machines," *IEEE Trans. Ind. Electron.*, vol. 58, no. 9, pp. 3815–3824, Sep. 2011.

[12] W. T. Villet and M. J. Kamper, "Variable-gear EV reluctance synchronous motor drives—An evaluation of rotor structures for position-sensorless control," *IEEE Trans. Ind. Electron.*, vol. 61, no. 10, pp. 5732–5740, Oct. 2014.

[13] A. Tüysüz, C. Zwyssig, and J. W. Kolar, "A novel motor topology for high-speed micro-machining applications," *IEEE Trans. Ind. Electron.*, vol. 61, no. 6, pp. 2960–2968, Jun. 2014.

[14] A. Tüysüz, M. Schöni, and J. W. Kolar, "Novel signal injection methods for high speed self-sensing electrical drives," in *Proc. IEEE Energy Convers. Congr. Expo. (ECCE)*, Sep. 2012, pp. 4663–4670.

[15] Y. Wang, S. L. Ho, W. N. Fu, and J. X. Shen, "A novel rotor position detection method for sensorless control of magnetic-geared permanent-magnet brushless motor," *IEEE Trans. Magn.*, vol. 49, no. 7, pp. 3961–3964, Jul. 2013.
[16] Celeroton AG. *Datasheet CM-2-500* [Online]. Available: www.celeroton.com, accessed Sep. 2015.
[17] Celeroton AG. *Datasheet CC-75-400* [Online]. Available: www.celeroton.com, accessed Sep. 2015.

Arda Tüysüz (S'10–M'13) received the B.Sc. degree in electrical engineering from Istanbul Technical University, Istanbul, Turkey, in 2006, the M.Sc. degree in electrical power engineering from RWTH Aachen University, Aachen, Germany, in 2009, and the Ph.D. degree in electrical drives from the Swiss Federal Institute of Technology (ETH) Zurich, Zurich, Switzerland, in 2015.

He is currently a Post-Doctoral Researcher with the Power Electronic Systems Laboratory, ETH Zurich. His research interests include novel electrical machine topologies, self-sensing control of high-speed electrical machines, and wide-bandgap power devices for very efficient and compact electrical drive systems.

Johann W. Kolar (M'89–SM'04–F'10) received the M.Sc. degree in industrial electronics and the Ph.D. degree (*summa cum laude*) in power electronics from Vienna University of Technology, Vienna, Austria, in 1997 and 1998, respectively.

He was appointed a Professor and the Head of the Power Electronic Systems Laboratory, Swiss Federal Institute of Technology, Zurich, Switzerland, on February 1, 2001. He has proposed numerous novel converter topologies and modulation/control concepts, e.g., the VIENNA rectifier, the SWISS rectifier, the delta-switch rectifier, and the three-phase ac–ac sparse matrix converter. He has authored/coauthored over 650 scientific papers published in international journals and conference proceedings and has filed more than 120 patents. His research interests include ultra-compact/efficient ac–ac and ac–dc converter topologies employing latest power semiconductor technology (SiC or GaN), solid-state transformers for smart microgrid systems, ultra-high speed and bearingless motors, and multidomain/scale modeling and multiobjective optimization.